Received November 19, 2021, accepted December 6, 2021, date of publication December 16, 2021,
date of current version January 10, 2022.

Digital Object Identifier 10.1109/ACCESS.2021.3136203

In-Loop Adaptive Filters to Improve the Power Quality of Switched Reluctance Generator in WECS

ELMER O. HANCCO CATATA[1,2], (Member, IEEE), PEDRO JOSE DOS SANTOS NETO[2,3], (Member, IEEE), MARCELO VINÍCIUS DE PAULA[4], (Member, IEEE), JOÃO PEDRO CARVALHO SILVEIRA[2], (Member, IEEE), TÁRCIO ANDRÉ DOS SANTOS BARROS[4], (Member, IEEE), AND ERNESTO RUPPERT FILHO[2], (Member, IEEE)

[1]Electrical Engineering Department, Federal University of Acre, Rio Branco-AC 69920-900, Brazil
[2]Faculty of Electrical and Computer Engineering, University of Campinas, Campinas-SP 13083-970, Brazil
[3]Faculty of Electrical Engineering, Federal University of Uberlândia, Uberlândia-MG 38408-100, Brazil
[4]Faculty of Mechanical Engineering, University of Campinas, Campinas-SP 13083-970, Brazil

Corresponding author: Elmer O. Hancco Catata (elmerhc110@gmail.com)

This work was supported in part by the São Paulo Research Foundation (FAPESP) under Grant 17/21640-9, Grant 16/08645-9, and Grant 17/21087-8; and in part by the National Council for Scientific and Technological Development (CNPq) under Grant 426404/2018-1.

ABSTRACT In this work, a proposal is presented to mitigate the voltage ripple effect generated by switched reluctance generator (SRG) in wind energy conversion systems (WECS). Voltage and current oscillations of switched reluctance generators are an expected consequence of the machine's natural switching operation. This switching operation creates a known frequency component, named stroke frequency. When the SRG is connected to the AC utility grid in WECS, these oscillations may compromise the generated power quality by introducing stroke frequency components in the grid electric current. To solve such issue, this work has as an original contribution the proposal of in-loop adaptive filters applied to mitigate the propagation of the SRG stroke frequency content in the DC-bus voltage of a grid-connected WECS. The notch cascading and moving average filters are implemented at the voltage loop of the voltage source converter in an adaptive form, as function of the SRG speed. Simulation and experimental results show that the waveform distortion of the injected electric current is greatly reduced compared to the conventional non-filtered SRG connection.

INDEX TERMS Switched reluctance generator, wind systems, adaptive filter, harmonic suppression filters, stroke frequency, voltage ripple frequency.

NOMENCLATURE

i_{og}	SRG generated output current [A].
v_{og}, v_{DC}	SRG generated output voltage and DC-link voltage [V].
C_{in}	DC-link capacitor [F].
L_f	VSC output filter [H].
v_a, v_b, v_c	Three-phase grid voltages [V].
i_a, i_b, i_c	Three-phase grid currents [A].
v_d, v_q, i_d, i_q	Direct and quadrature axis voltage [V] and current [A].
v_a^*, v_b^*, v_c^*	Three-phase PWM output voltages.
i_d^*, i_q^*	Direct and quadrature axis current [A] reference.
θ	AC grid synchronism angle [°]
ω_g	Grid (electrical) speed, corresponding to the time derivative of θ.
P, Q	VSC active [W] and reactive [VAr] power.
P^*	VSC reactive power reference [VAr].
P_g, P_g^*	SRG generated mean power and reference power [W].
$I_{a,b,c}$	SRG phase currents [A].
I^*	SRG phase current reference [A].
$S_{a,b,c}$	Switching pulses for AHB converter.
θ_{on}, θ_{off}	SRG firing angles [°]
ω	SRG speed [rad/s].
k_p,k_i	VSC internal current control i_d, i_q coefficients.

The associate editor coordinating the review of this manuscript and approving it for publication was Chandan Kumar.

ω_v, PM	DC-link voltage compensator coefficients.
F_{st}	Stroke frequency [Hz].
$\xi_1, \xi_2, \lambda_1, \lambda_2$	ANF coefficients.
ω_c	Filters cut-off frequency [rad/s].
T_d	Discrete sampling period [s].
T_w, N_f, N_c	MAF window length, rounding-down and rounding-up MAF order.

I. INTRODUCTION

The switched reluctance generators (SRG) have drawn attention for robustness as no winding or magnets is present on the rotor, besides the machine's low cost and high efficiency. The SRG advantages make these machines suitable for variable speed applications, such as in electric vehicle and wind energy conversion system (WECS) [1]–[3]. However, the SRG switching operation results in output voltage and current oscillations, leading to power quality issues in grid-connected WECS applications.

Different researchers have studied the issue of the SRG output voltage ripple. In [4], a control system is implemented, in which the voltage ripple is preprocessed to close the voltage control loop. For the voltage measurement, two methods are proposed by the authors. The first method is based on a low-pass filter, in which the cutoff frequency is adapted according to the SRG operating speed. In the second method, the control is sampled synchronously with the rotor position, resulting in the reduction of the output voltage ripple. In [5], a sufficiently large capacitor was applied to decrease the DC-link voltage oscillations. This large capacitor is designed taking into account the stroke frequency at specific operating points. In [6], a boost converter is applied for actively filtering the SRG source current to avoid the usage of a bulk capacitor bank. With this method, a higher reduction of the SRG output voltage oscillation is achieved using a reduced size capacitor.

SRG-based WECS inject power into the electrical grid under a variable speed operation, as discussed by the following works. In [2], the SRG output power is controlled using an asymmetric half-bridge (AHB) converter to deliver the generated power to the electrical grid. Among the results, the authors discuss the voltage ripple only to design the capacitor bank. In [1], the SRG is connected to the utility grid through a C-dump converter. In addition, voltage and power control are applied to the generator. In [7], [8], simulations of a speed-control system were performed using an adaptive neural network. This strategy acts over the current control of an SRG connected to the electrical grid using a voltage source converter (VSC). In [9], a control system for SRG applied in wind power generation was presented, in which a current controller was applied to adjust the SRG generated power. In addition, a buck converter was used as an interface between the inverter connected to the electrical grid and the SRG, since the generator was designed to operate with a voltage lower than the DC-link. In [10], [11], a WECS composed of a dependent excited SRG connected to the electrical grid through a single-phase inverter was studied. Therefore, the previous works do not show voltage ripple details and the effects on the quality of the power sent to the utility grid.

Due to the existence of the switching operation in the generation process, the SRG output voltage inevitably has oscillations with frequencies directly proportional to the SRG operating speed; low frequencies for low speeds and the frequency increases proportionally to the SRG speed. In SRG-WECS the DC-bus voltage ripple is propagated through the VSC voltage controller. Consequently, the active power reference is affected by the SRG output voltage oscillations, resulting in current waveform distortion on the electrical grid. This is a detrimental effect, since the achievable performance may decrease below an acceptable level, regarding the harmonic content in the grid [12]. For this reason, this paper proposes in-loop filtering methods to improve the power quality of the grid-connected SRG. These methods are based on suppressing the voltage oscillations in the DC-link loop caused by the SRG switching operation. Two different strategies for ripple suppression are discussed, the notch cascading filters and moving average filter.

The paper is organized as follows: The mathematical model of the SRG, the VSC and the voltage ripple propagated to the grid current are described first. The procedures of current and voltage compensator design are described for VSC, followed by the stability analysis of the inserted filters in cascade with the voltage compensator in the dc-link. The effectiveness of the proposed methods applied at fixed operating speeds is demonstrated, for speeds below and above the SRG base speed; then, the adaptive forms of these filters for variable speed operation are validated. The experimental results show that the proposed strategies reduce the waveform distortion of the injected current, thus improving the power quality of the SRG-based wind system when compared to a non-filtered solution.

II. SRG MATHEMATICAL MODEL AND OPERATION

Disregarding the saturation, the SRG electrical equation per phase is given by:

$$v_{og}(t) = Ri(t) + \frac{d}{dt}\psi(\theta, i) \tag{1}$$

in which v_{og} is the SRG output voltage, R is the copper resistance, i is the electric phase current, ψ is the magnetic flux, and θ is the rotor position. If the inductance is linearly varying with rotor position, the electromagnetic torque T_e, is given by:

$$T_e(t) = \frac{i(t)^2}{2}\frac{dL(\theta, i)}{d\theta} \tag{2}$$

in which L is the self-inductance dependent on the rotor position and phase current. Extending (1) using $\psi(\theta, i) = L(\theta, i)i(t)$ and disregarding flux saturation, the SRG electrical and mechanical equations yields:

$$v_{og}(t) = Ri(t) + i(t)\omega(t)\frac{dL(\theta, i)}{d\theta} + L(\theta, i)\frac{d}{dt}i(t) \tag{3}$$

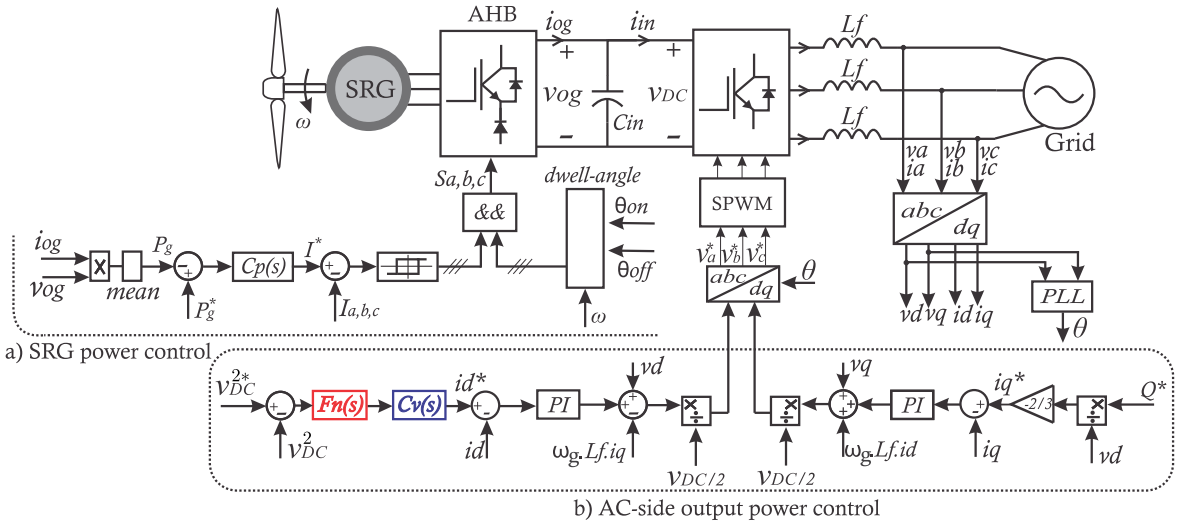

FIGURE 1. SRG-based wind conversion system connected to the utility grid. Detail a) depicts the SRG control. Detail b) depicts the VSC control, including the in-loop adaptive filter.

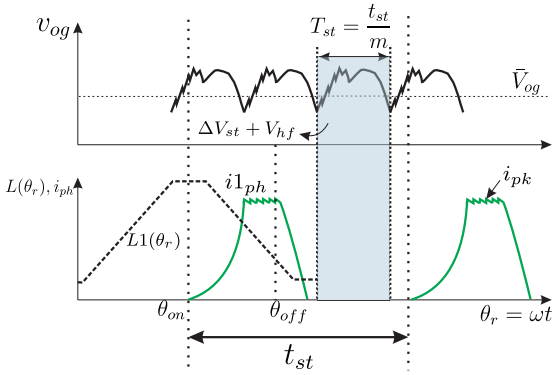

FIGURE 2. SRG output voltage ripple and generation process waveforms.

$$\frac{i(t)^2}{2}\frac{dL(\theta,i)}{d\theta} - T_l = J\frac{d\omega(t)}{dt} + B\omega(t) \tag{4}$$

in which ω is the rotor speed, T_l is the load torque, J is the inertia coefficient, and B is the friction coefficient. Thus, using (3) and (4), it is possible to design the control scheme, as shown in Fig. 1.a.

The generation process consists of two stages: in the first stage, the stator is magnetized starting from θ_{on} to θ_{off} in the area where the inductances decrease (Fig. 2). During this period, the input mechanical and electrical energy are converted into stored electromagnetic energy. In the second stage, this energy is released to DC-link capacitor through the AHB converter's diodes.

III. SRG OUTPUT VOLTAGE RIPPLE

The typical SRG instantaneous output voltage waveform is composed of the following terms [13]:

$$v_{og} = \bar{V}_{og} + \Delta V_{st} + \Delta V_{hf} \tag{5}$$

where $\bar{V}_{og}$ is the average value, ΔV_{st} is the stroke ripple component due to phase commutation, and ΔV_{hf} is the high frequency switching component, as shown in the upper side of Fig. 2. The voltage ripple frequency (F_{st}) and respective harmonics depend on the generator operating speed, as shown in [14].

$$F_{st} = mf_{st} = m\frac{\omega N_r}{2\pi} \tag{6}$$

where F_{st} is m times the stroke frequency (f_{st}), m is the SRG number of phases, N_r is the rotor poles and ω is the SRG speed, as described in Fig. 2, where the inductance profile, the phase current and the voltage ripple with their components are shown.

The mechanical speed delivered to the wind turbine is variable, hence the machine operates at a variable speed. This implies that the stroke frequency presented in the SRG output voltage is also variable. Thus, the average voltage has to be measured taking into account the stroke frequency.

Computing F_{st} by using (6), the DC-link capacitor can be determined according to the lower voltage ripple frequency as:

$$C_{in} = \frac{P_g}{v_{og}\Delta v_{og} 2m\,\omega N_r} \tag{7}$$

where P_g is the nominal power and Δv_{og} is the voltage ripple.

IV. SRG IN WECS CONNECTED TO THE UTILITY GRID

In WECS applications, the SRG wind turbine is connected to the utility grid as shown in Fig. 1. This topology of connection to the electrical grid, including the SRG and a VSC, has been developed and tested in previous works [2], [9], [10]. An asymmetric half-bridge converter drives the SRG. Fig. 1.a depict the SRG control; the SRG current is controlled by hysteresis and single pulse for low and high operating speeds, respectively. The SRG control regulates the extraction of

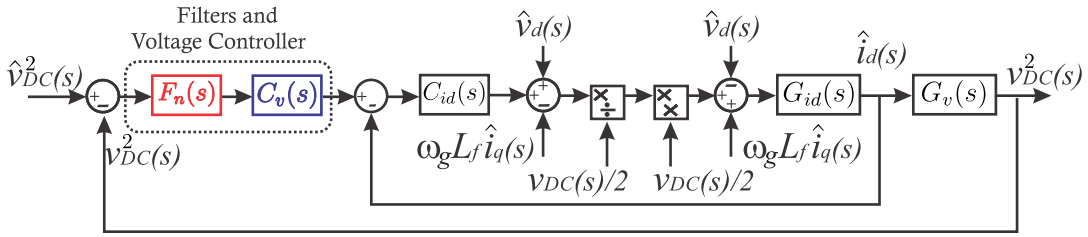

FIGURE 3. Linearized, decoupled model of the $i_d(s)$ current and DC-side voltage control of VSC.

the maximum electric power according to the wind profile by using a direct power control [2]. The VSC control is performed in the synchronous reference frame. The VSC is responsible for regulating the DC-link voltage and sending the SRG generated power to the utility grid. Fig. 1.b depicts the VSC control, in which the proposed adaptive filters are emphasized in the voltage control loop.

A. VSC CONTROL IN THE SYNCHRONOUS REFERENCE FRAME

For an appropriate VSC operation, the DC-side voltage has to be adequately controlled during the transient and steady states. For this purpose, the VSC accurate modeling is necessary. An accurate model of the VSC DC-side voltage is developed in [15], which is replicated in this paper.

1) VOLTAGE CONTROL

The transfer functions of the direct, i_d, and quadrature, iq, current components are initially obtained from the Park transform for the VSC vectorial equations, as detailed in [16]. The SRG delivers the controlled power to the DC-bus, while the DC-bus voltage is freely developed if no control regulation is performed. Thus, the power balance in the DC-bus is expressed by (8), as function of the VSC active and reactive powers.

$$\frac{C_{in}}{2}\frac{dv^2_{DC}}{dt}(t) = p_g(t) - p_s(t) - \frac{2L_f}{3\hat{V}_s^2} \times \left[p_s(t)\frac{dp_s(t)}{dt} - q_s(t)\frac{dq_s(t)}{dt}\right] \quad (8)$$

where C_{in} is the DC-bus capacitance, v_{DC} is the DC-link voltage, p_g is the external SRG generate power, p_s is the utility grid active power, q_s is the utility grid reactive power, L_f is the output filter inductance, and $\hat{V}_s$ is the grid peak phase voltage.

Equation (8) is nonlinear due to the terms $p_s(t)\dfrac{dp_s(t)}{dt}$ and $q_s(t)\dfrac{dq_s(t)}{dt}$, which are linearized at a specific operating point, such as $p_s(t) = P + \hat{p}_s(t)$ and $q_s(t) = Q + \hat{q}_s(t)$, resulting in:

$$\frac{C_{in}}{2}\frac{d\hat{v}^2_{DC}}{dt}(t) = \hat{p}_g(t) - \hat{p}_s(t) - \frac{2L_f}{3\hat{V}_s^2}\left(P\frac{d\hat{p}_s(t)}{dt} - Q\frac{d\hat{q}_s(t)}{dt}\right) \quad (9)$$

where P and Q are the active and reactive power at a specific operating point.

By applying the Laplace transform in (9), and assuming $\hat{v}^2_{DC}(s)$ as a state variable, then one has the transfer function for voltage control:

$$\left.\frac{\hat{v}^2_{DC}(s)}{\hat{p}_s(s)}\right|_{\hat{p}_g,\hat{q}_s=0} = \frac{-2\left(1 + \dfrac{2L_f Ps}{3\hat{V}_s^2}\right)}{C_{in}s} \quad (10)$$

Based on what has been previously described, Fig. 3 shows the current control diagram of the direct component, i_d, which was linearized and decoupled along with the external voltage control loop on the DC-side. The current compensator $C_{id}(s)$ is composed by PI controller and designed to ensure that there is no overshoot based on the plant poles with $k_p = 62.8319$ and $k_i = 3.7699e3$.

From Fig. 3, closing the current control loop, the open loop transfer function of DC-link voltage is expressed as:

$$G_{vOL}(s) = C_v(s)G_{idCL}(s)G_v(s) \quad (11)$$

in which $C_v(s)$ is the Dc-link voltage compensator, $G_{idCL}(s)$ is the inner closed-loop current control, and $G_v(s)$ is the transfer function that relates active power to DC-link voltage.

To control DC-link voltage, the compensator $C_v(s)$ is composed by an integrator witch is used to guarantee ramp and unity step tracking, followed by a lead compensator to incorporate the desired phase margin boost.

B. SRG-WECS SIMULATION WITH NO HARMONIC SUPPRESSION

By applying the Park transform in the voltage and current signals with frequency f_o, the output dq signals are shifted in frequency [17], [18]. The harmonics order that appears in the three-phase system are shifted $\pm f_o$ in respect to the voltage ripple frequency, F_{st}. Fig. 4 shows the grid current and its spectrum when the generator operates at a minimum speed of 600 rpm, and power of 300 W.

The minimum speed is chosen based on the system efficiency. In this situation, the voltage ripple frequency components that appear in the utility grid current are given according to (12). The voltage ripple frequency appear in pairs after the fundamental as $hF_{st} \pm f_o$: $1F_{st} \pm f_o$ for the voltage ripple first harmonic; $2F_{st} \pm f_o$ for the voltage

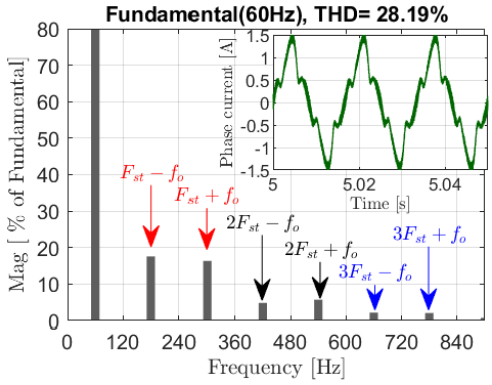

FIGURE 4. Simulated grid current and harmonic at 600 *rpm* and 300 *W*.

ripple second harmonic; $3F_{st} \pm f_o$ for the voltage ripple third harmonic, and so on. These contents will continue to appear in pairs according to (12) as shown in Fig. 4, where $F_{st} = 240$ Hz belongs to 600 rpm of generator speed according to (6). In (12), F_h is the voltage undulation frequency harmonic that appear in the grid current. F_{st} is the output voltage undulation frequency or named as stroke frequency component in this paper, f_o is the grid frequency, and h is the voltage undulation harmonic order.

$$F_h = hF_{st} \pm f_o, \quad (h = 1, 2, 3 \ldots) \tag{12}$$

V. PROPOSED FILTERING SOLUTIONS

In this section, two in-loop filtering solutions are proposed to mitigate the effect of the SRG stroke frequency content at the VSC DC-side. These filters are inserted in the VSC voltage control loop to avoid frequency content propagation towards the AC utility grid. Consequently, the power quality of the SRG system can be significantly enhanced.

A. ADAPTIVE NOTCH FILTER (ANF)

To suppress the SRG voltage ripple frequency, F_{st}, in the VSC voltage loop, the adaptive notch filter are designed for -60 dB of depth and 40 Hz of bandwidth, such as:

$$G_{nf}(s) = \frac{(s/\omega_c)^2 + 2\xi_1 s/\omega_c + 1}{(s/\omega_c)^2 + 2\xi_2 s/\omega_c + 1} \tag{13}$$

where $\omega_c = 2\pi h F_{st}$(for h = 1) is the notch filter center frequency and depends on the voltage ripple frequency, ξ_1 and ξ_2 are coefficients that define the band and notch depth, respectively. This, in order to avoid grid current harmonics in $1F_{st} - f_o$ and $1F_{st} + f_o$.

As previously observed in Fig. 4, the most prominent frequency components of the voltage ripple are $h = 1, 2$. However, higher-order components distant from the fundamental frequency may appear. For $h = 2$ of F_{st}, a second notch filter is projected; with central frequency at $\omega_c = 2\pi 2F_{st}$, with depth and band defined by λ_1 and λ_2 respectively. This in order to avoid grid current harmonics in $2F_{st} - f_o$ and $2F_{st} + f_o$.

By inserting a cascade of two notch filters, $G_{nf1}(s)$ (for $h = 1$) and $G_{nf2}(s)$ (for $h = 2$), into the direct path of the VSC voltage loop, the open-loop transfer function (11) is modified as:

$$T_v^{nf}(s) = G_{nf1}(s)G_{nf2}(s)C_v(s)\, G_{vOL}(s) \tag{14}$$

Fig. 5(a) presents the superposition of (11) and (14) with cascaded notch filters at 600 rpm and 1500 rpm. That corresponds to the total open loop voltage transfer function without filter and with cascaded filter inserted in two situations: for minimum operation speed of 600 rpm, the cascaded notch filters are situated at 240 Hz, 480 Hz. For nominal speed of 1500 rpm, situated at 540 Hz and 660 Hz. It is clearly observed that at low speeds the filter has a greater phase shift than at high speeds.

The discrete form of the adaptive filter using the bilinear transformation can be derived from (13). Keeping ξ_1, ξ_2 and λ_1, λ_2 fixed and varying $h\omega_c$, for $h = 1, 2$, the first adaptive notch filter in the discrete form is given by:

$$Gnf(z) = \frac{a_0(\omega_c) + a_1(\omega_c)z^{-1} + a_2(\omega_c)z^{-2}}{1 + a_1(\omega_c)z^{-1} + b_2(\omega_c)z^{-2}} \tag{15}$$

where $a_0(\omega_c)$, $a_1(\omega_c)$, $a_2(\omega_c)$, $b_2(\omega_c)$ are coefficients that depend on the output voltage frequency variation, with parameters provided in appendix A.

B. ADAPTIVE MOVING AVERAGE FILTER (AMAF)

The moving average filter (MAF) can act as low-pass filter if certain conditions hold. MAF transfer function is defined as:

$$G_{MAF}(s) = \frac{1 - e^{-T_\omega s}}{T_\omega s} \tag{16}$$

where T_ω is the window length.

The transfer function (16) provides unity gain at zero frequency, and zero gain at frequencies $f = n/T_\omega$ ($n = 1, 2, 3, \ldots$). This means that the MAF passes the low frequency components and completely attenuates integer multiples of $1/T_\omega$. To analyze the stability in the DC-link control loop, the MAF lag must be estimated [19]. A second order Padé approximation is applied, such as:

$$e^{-T_\omega s} \cong \frac{12 - 6T_\omega s + (T_\omega s)^2/12}{12 + 6T_\omega s + (T_\omega s)^2/12} \tag{17}$$

Thus, the second-order Padé approximation transfer function of the MAF filter is expressed as:

$$G_{MAF_p}(s) \cong \frac{1}{1 + T_\omega s/2 + (T_\omega s)^2/12} \tag{18}$$

The Bode graph of the open-loop voltage control $GcvOL(s)$, with $G_{MAF}(s)$ inserted, is shown in Fig. 5(b); where the $G_{MAF}(s)$ was designed for the SRG operation at 600 rpm. In Fig. 5(b), the magnitude peaks down at $G_{MAF}(jh2\pi/T_w)$ with $h = 1, 2, 3, \ldots$, according to the voltage ripple frequency harmonic order. Unlike the notch filter, MAF is also able to filter the consecutive harmonics of the SRG voltage ripple frequency, with window length $T_w = 1/F_{st}$.

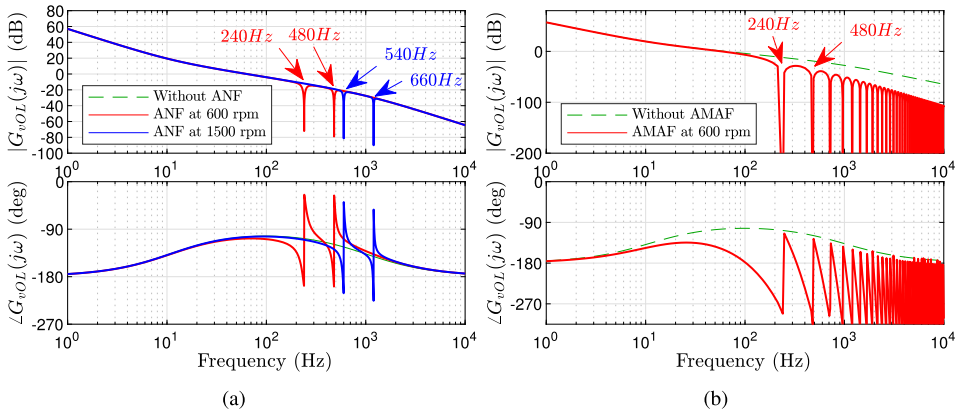

FIGURE 5. Bode diagram of the voltage open-loop TF without and with cascaded filters set at $F_{st} = 240$ Hz and $2F_{st} = 480$ Hz for 600rpm; for 1500 rpm set at $F_{st} = 540$ Hz and $2F_{st} = 660$ Hz, a) $G_{vOL}(s)$, and $T_v^{nf}(s)$ with $\xi_1 = 8.3333e-5$, $\xi_2 = 0.0833$ and $\lambda_1 = 4.1667e-5$, $\lambda_2 = 0.0417$, for 600 rpm, also, $\xi_1 = 3.3333e-05$, $\xi_2 = 0.0333$ and $\lambda_1 = 1.6667e-05$, $\lambda_2 = 0.0167$, for 1500 rpm b) $G_{vOL}(s)$, and $T_v^{MAF}(s)$ with $T_w = 1/F_{st}$ for 600 rpm.

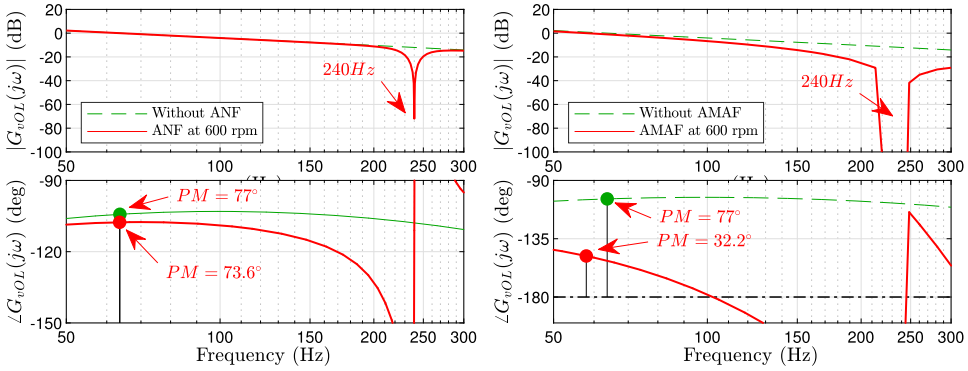

FIGURE 6. Stability analysis of the VSC voltage open-loop TF, at the critical SRG speed of 600 rpm and positive nominal rated power, with and without the proposed adaptive filters. a) ANF; b) AMAF.

By adding a MAF to the voltage loop, the open-loop voltage transfer function is expressed as:

$$T_v^{MAF}(s) = G_{MAF}(s)G_{vOL}(s) \tag{19}$$

By substituting the second-order approximation (18) into (19), the open-loop transfer function can be approximate as:

$$T_v^{MAF_p}(s) \cong G_{MAF_p}(s)G_{vOL}(s) \tag{20}$$

It was verified that MAF second-order Padé approximation yields better results than the first-order approximation for low frequencies of the voltage ripple, since it accompanies most of the MAF lag. Hence, the second-order approximation allows to properly choose the voltage controllers' phase margin boost.

To achieve frequency-adaptive MAF, many approaches are proposed in the literature [19], [20]. In this work, the MAF online adjustment through its window length is adopted, according to the SRG voltage ripple frequency variations, F_{st}. The AMAF window length is adapted to the F_{st} by adjusting the MAF order, N. The weighting mean value (WMV) approach is used to make the MAF frequency adaptive [21], such as:

$$\bar{x}(k) = \frac{1-\alpha}{N_f}\sum_{i=0}^{N_f-1} x(k-i) + \frac{\alpha}{N_c}\sum_{i=0}^{N_c-1} x(k-i) \tag{21}$$

where $N_f = floor(T_w/Td)$, $N_c = ceil(T_w/Td)$ are the rounding-down and rounding-up MAF order, respectively; T_d is the discrete sampling frequency, and α is called the weighting factor, given by:

$$\alpha = \frac{1}{F_{st}T_d} - N_f \tag{22}$$

For a given window length, T_w, the discrete transfer function of (21) can be represented as:

$$G_{MAF}^{WMV}(z) = \frac{\frac{1-\alpha}{N_f} + \frac{\alpha}{N_f+1} - \frac{1-\alpha}{N_f}z^{-N_f} - \frac{\alpha}{N_f+1}z^{-(N_f+1)}}{1-z^{-1}} \tag{23}$$

VI. DC-LINK VOLTAGE COMPENSATOR DESIGN APPROACH AND STABILITY ANALYSIS

The voltage compensator phase margin is designed according to the phase delay of the inserted filters $F_n(s)$. Hence, the compensated open-loop transfer function, including the voltage controller and proposed filters, which is expressed as:

$$G_{cvOL}(s) = C_v(s)F_n(s)G_v(s)G_{idCL}(s) \tag{24}$$

To design the compensator, let us consider the worst-case scenario that corresponds to AMAF filter at minimum SRG operation speed(600 rpm), which was determined in studies prior to the voltage compensation. Taking as reference DC-link voltage control procedures in [16], and considering that the inner current compensator delay is negligible with $\omega_v = \omega_i/10$. First the phase margin and gain crossover frequency are fixed at 45° and 700 rad/s for worst-case scenario that corresponds to negative rated active power. Fig. 7 shows that at negative nominal power with AMAF filter inserted, the phase margin falls for $PM = -17°$, thereby, the lead compensator boost is increased to 70° for positive nominal active power, and the controller crossover frequency has to be placed further away from the frequency range where the AMAF will move. Hence, the phase margin characteristics are improved by $\omega_v = 400$ such that PM is equal to 15°, 24°, 32°, for negative nominal active power, zero power, positive rated active power, respectively.

When adding the cascade notch filters (600 rpm) into the voltage loop with previously projected compensator, the phase margin is 53° for negative nominal power. Thereby, stability at nominal power is guaranteed with $PM = 73.6°$, as shown in Fig. 6(a). Fig. 6(b) shows the superimposed bode plot of the open-loop transfer functions $G_{vOL}(s)$ and $T_v^{MAF}(s)$. It is possible to notice that the open-loop TF without the AMAF has 77° of phase margin; while with the AMAF at 600 rpm, the phase margin is reduced to 32.2°. Notably, the AMAF transfer function, $G_{MAF}(s)$, introduces a significant phase at low frequencies, reducing the phase margin at the crossover frequency, and weakening the stability of the voltage loop considerably. Still, the voltage loop remains stable.

VII. EXPERIMENTAL RESULTS

For experimental confirmation of the proposed voltage ripple frequency filtering methods in SRG WECS, an experimental setup Fig. 9 was assembled. A 2.2 kW three-phase induction motor (IM) was coupled to the SRG to emulate a wind turbine. The IM operating speed is controlled through a frequency inverter. The SRG and IM are connected by a torque transducer model HBMT22/50NM. A central control board was developed using a digital signal processor (TMS320F28335), signal conditioning circuits, protection and isolation circuits. *LEM* sensors were used to measure current (LA55-P) and voltage (LV20-P). The acquirement of currents, voltages and speed were obtained by means of a *National Instruments* NI-6259 data acquisition (DAQ) board and a software interface was developed in Labview.

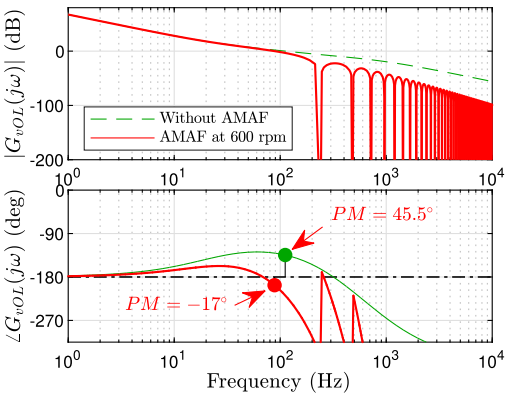

FIGURE 7. Bode plot of the DC-link voltage loop gain at negative rated active power with: $C_{in} = 1200e-6$, $\omega_v = 700$ rad/s, $L_f = 10$ mH, $P_s = -2$kW, $\hat{V}_s = 179.6292$ V, lead compensator boost = 68°.

TABLE 1. Test-stand specifications and control parameters.

SRG parameters:	values	unit
Nominal speed	1500	rpm
Nominal power	$2k$	W
Poles(stator / rotor)	$12/8$	-
Resistance of stator	4.3	Ω
Supply voltage	400	V
VSC current control parameters:		
Cutoff frequency	$6.2832e3$	rad/sec
Phase margin	90	(°)
Switching frequency	10	kHz
L filter	10	mH
VSC DC-link control parameters:		
Link capacitor	2.25	uF
Cutoff frequency	400	rad/s
Phase margin(for nominal power)	77	(°)

A 12-bit resolution, 400 MHz *Lecroy* oscilloscope was used for data acquisition and *Matlab* software for data processing. The controllers were discretized at 40kHz and computed in the DSP. Table 1 presents the test-stand specifications and control parameters used in this work.

The Fig. 8 shows the grid current spectrum without filter inserted and SRG operating at different speeds. Fig. 8(a) shows the components of F_{st} in pairs up to $h = 3$ for SRG at 600 rpm. Fig. 8(b) shows F_{st} in pairs up to $h = 2$ for SRG at 900 rpm. Also, Figs.8(c,d) show the components for F_{st} at 1300 rpm and 1500 rpm respectively, in which the components for $h = 2, 3, \ldots$ are further away of the displayed frequency range.

A. SRG OPERATING BELOW THE BASE SPEED

The experimental results of the voltage ripple filtering are presented in Fig. 12. In this situation, the SRG current is controlled by hysteresis. The grid current, the grid voltage, the SRG phase current, and the trigger signal are shown. The trigger activates the proposed filters to observe the grid currents. On the other hand, on the bottom side of each figure, the grid current spectrum is showed using the FFT. In which,

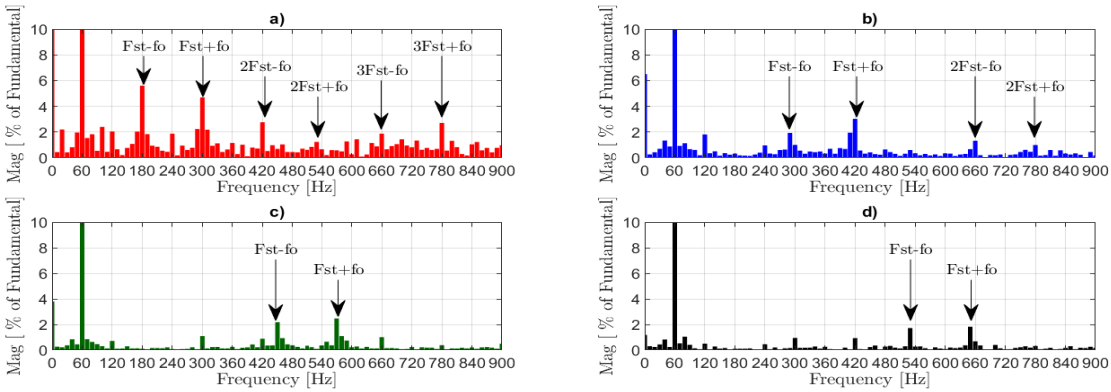

FIGURE 8. Unfiltered grid current FFT anlysis: a) FFT spectrum at 600 rpm; b) FFT spectrum at 900 rpm; c) FFT spectrum at 1300 rpm; d) FFT spectrum at 1500 rpm.

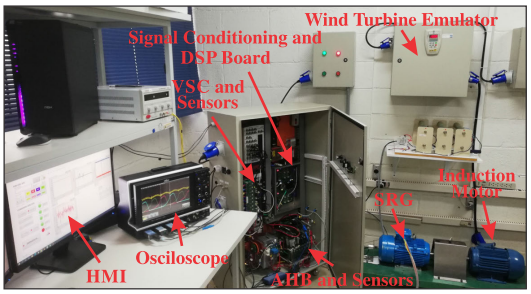

FIGURE 9. Experimental setup of a SRG based WECS.

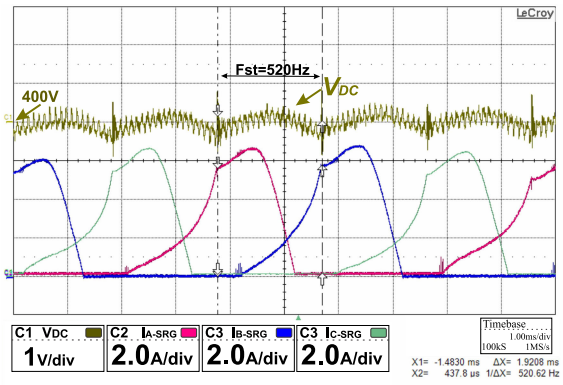

FIGURE 10. DC-link voltage and SRG phase current.

the voltage ripple frequency components at $1F_{st} \pm f_o$ are shown in unfiltered and filtered situations.

To verify the effectiveness of the proposed filters, firstly, the system in Fig. 1 is controlled without any filters. After the trigger signal, the filters are inserted and automatically tuned at $1F_{st}$ and $2F_{st}$ for avoid $1F_{st} \pm f_o$ and $2F_{st} \pm f_o$ frequencies in the grid current for respective SRG operating speed. Figs. 12(a) and 12(b) show the behavior of the electrical current (red signal) injected into the grid, before and after the adaptive filter is inserted for 900 rpm. It is noticeable a reduction of the waveform distortion. The current frequency component magnitudes are displayed on the bottom of each figure. A comparison between unfiltered and filtered grid current spectrum illustrates the effectiveness of the proposed

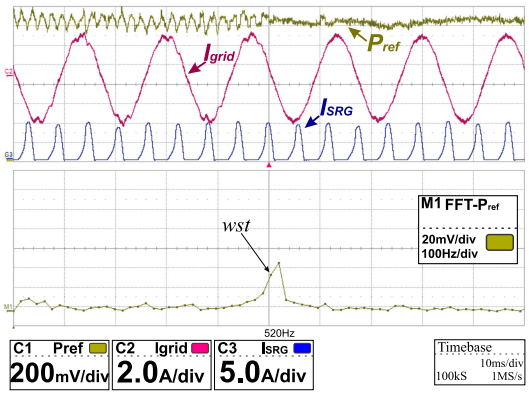

FIGURE 11. VSC active power reference, grid current, and SRG phase currents at 1300 rpm,1200w.

filters. It is possible to verify that the SRG voltage ripple frequencies at 300 Hz and 420 Hz for 900 rpm are attenuated by 63.3 dB, and 62.4 dB, when the MAF, and ANF are applied, respectively.

The Fig. 13 shows the experimental result of the grid current spectrum for 600 rpm. In which, it can be seen that apart from the components of F_{st} other components appear, such as: f_2; f_5, f_7, f_{11}, f_{13} which correspond to a slight imbalance in IM and in the grid voltage respectively.

Figs. 13(a), 13(b) show the results in inserted filters situations AMAF, ANF respectively. The filters are inserted at $F_{st} = 240$ Hz and $2F_{st} = 480$ Hz, in order to filter $F_{st} - f_o = 180$ Hz, $F_{st} + f_o = 300$ Hz and $2F_{st} - f_o = 420$ Hz, $2F_{st} + f_o = 540$ Hz respectively; it can be seen that the F_{st} and $2F_{st}$ components were effectively filtered, leaving only the components related to imbalances and the components of $3F_{st}$ for which no filters were inserted. Also, the AMAF filter leaves the spectrum cleaner than the ANF.

B. SRG OPERATING ABOVE THE BASE SPEED

The VSC power reference, grid current, SRG output current, and the VSC power reference spectrum using the fast Fourier transform (FFT) are presented in Fig. 11 for AMAF filter situation. The SRG operates in the single pulse mode at 1300 rpm and 1200 W, as shown by the current

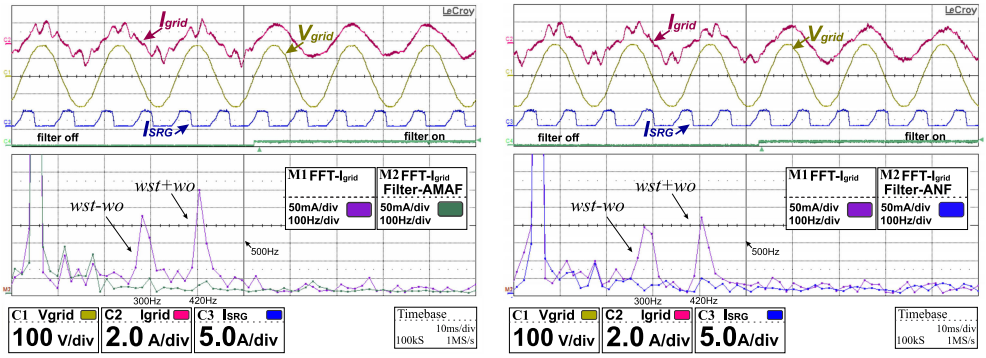

FIGURE 12. Experimental analysis of the proposed in-line adaptive filters at SRG low speed. a) AMAF, 900 rpm, 600 W; b) ANF, 900 rpm, 600 W.

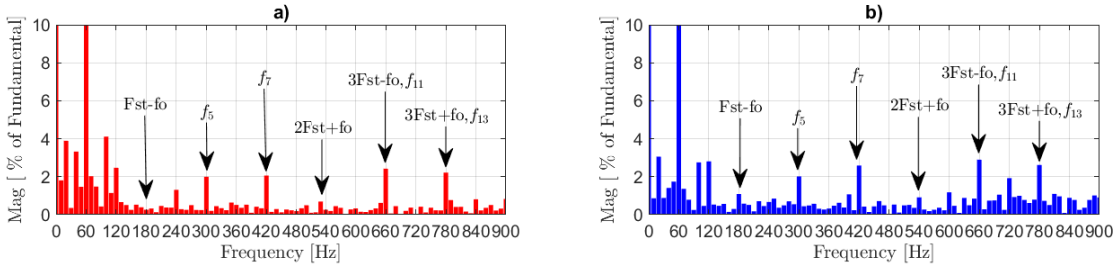

FIGURE 13. Filtered grid current FFT spectrum at 600 rpm: a) FFT spectrum with AMAF; b) FFT spectrum with ANF.

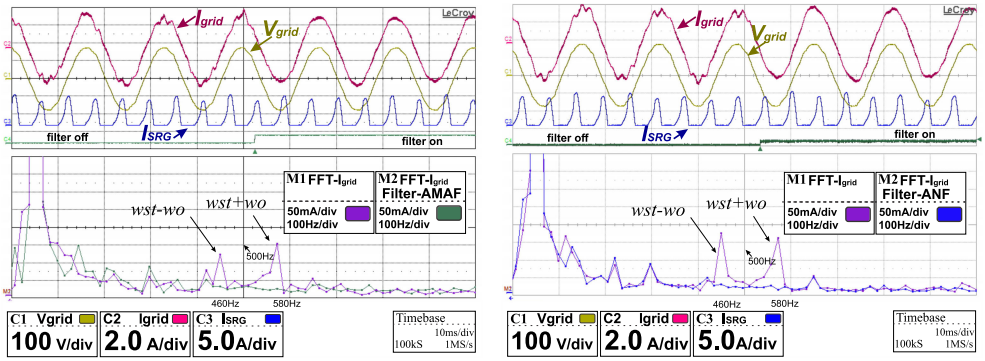

FIGURE 14. Experimental analysis of the proposed in-line adaptive filters at SRG high speed. a) AMAF, 1300 rpm, 1200 W; b) ANF, 1300 rpm, 1200 W.

waveforms. The VSC power reference spectrum is shown before the filter is activated, in which the voltage ripple F_{st} is observed at 520 Hz for 1300 rpm (Fig. 10), according to (6). The VSC power reference is distorted before the filter activation due to the stroke frequency component. Under these conditions, I_{grid} includes the grid and stroke harmonics, since V_{DC} contains the SRG output voltage ripple. When the tuned filters are activated, the stroke components are eliminated from the power reference. Consequently, this results in the I_{grid} stroke frequency component elimination.

Figs. 14(a), and 14(b) report the results obtained at 1300 rpm. The generator is controlled through voltage single pulse. The SRG stroke frequency components that appear in the grid current occur at 460 Hz and 580 Hz. The AMAF experimental behavior is presented in Fig. 14(a). One can see that the grid current waveform is improved since the stroke components are attenuated in approximately 15.5 dB by the in-line filter. The same experiment is reproduced for the ANF, as shown in Fig. 14(b). It is seen that the ANF also effective in attenuating the grid current distortion in approximately 16.9 dB.

Fig. 15 shows the spectrum for 1500 rpm in which the components at 540 Hz, 660 Hz were filtered remaining only f_5, f_7, f_{11}; It is possible to observe that for this nominal speed, the grid current waveforms is improved by the action of the filters and also by the contribution of the power reference level.

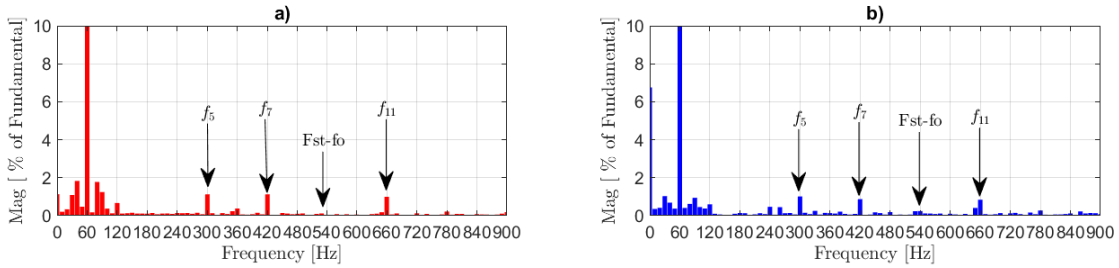

FIGURE 15. Filtered grid current FFT spectrum at 1500 rpm: a) FFT spectrum with AMAF; b) FFT spectrum with ANF.

TABLE 2. Grid current THD performance comparison.

$SRG - Speed$ (rpm)	MAF	$AMAF$
900	≈8.0 %	6.2 %
1200	≈4.6 %	2.3 %
1500	≈3.5 %	1.4 %

In addition, to observe the THD performance of the proposal addressed in this work, a conventional filtering methodology addressed in [14] is compared. The DC link voltage measurement is previously processed with a MAF filter with fixed cutoff frequency. The THD obtained was ≈ 8.0% for 900 rpm and ≈ 3.5% for 1500 rpm. Meanwhile, for the case using the proposed AMAF filter, the THD was 6.2% for 900 rpm and 1.4% for 1500 rpm. Table 2 summarizes a harmonic distortion comparison for speeds below and above the SRG base speed. From Table 2, it is possible to verify that the proposed methodology using adaptive filter in the voltage control loop shows its superiority.

VIII. CONCLUSION

This paper highlights the existence of stroke components in the electrical grid and the mathematical relationship with which they appear. For which, the paper has presented in-line adaptive filters, at the DC-link voltage control loop and the care that must be taken when inserting the filters together to the voltage compensator. The proposed filters were designed aiming to mitigate the SRG stroke frequency components that cause DC-link voltage ripple, thereby being propagated into the grid electric current. To verify the effectiveness of the proposed adaptive filters, the results were shown in two different speeds, in situation below the base speed and above the base speed. In both cases, the proposed adaptive filters have shown proper effectiveness remaining only components related to imbalances.

Also, the results showed that at low speeds and low power levels, it results in significant distortion in the grid current, and for the situation of high speeds with significant power levels, less distortion of the grid current. Even at high speeds, the stroke components appear distorting the grid current; for which the experimental results have shown that the two proposed filters effectively attenuate the grid current waveform distortion at low and high speeds, therefore the filtering methods were able to adaptively mitigate the frequencies related to the SRG stroke frequency.

The voltage controller was designed taking into account the phase lag added by the proposed filters at low speeds. The adopted design approach considers that the DC-link voltage compensator is calculated such that the inserted adaptive filters do not destabilize the voltage control loop at minimum operating speed. Therefore, the zero dB crossover frequency and phase margin of the DC-link voltage compensator were strictly limited in an acceptable range for the SRG low operation speeds. The stability analysis revealed that the system phase margin is less affected when the adaptive notch filter is inserted. Thus, the ANF filter yields a stabler behavior than the AMAF filter, however the MAF filter had better filtering than the cascade ANF filter.

REFERENCES

[1] R. Cardenas, R. Pena, M. Perez, J. Clare, G. Asher, and P. Wheeler, "Control of a switched reluctance generator for variable-speed wind energy applications," *IEEE Trans. Energy Convers.*, vol. 20, no. 4, pp. 781–791, Dec. 2005.

[2] T. A. D. S. Barros, P. J. D. S. Neto, P. S. N. Filho, A. B. Moreira, and E. R. Filho, "An approach for switched reluctance generator in a wind generation system with a wide range of operation speed," *IEEE Trans. Power Electron.*, vol. 32, no. 11, pp. 8277–8292, Nov. 2017.

[3] P. J. D. S. Neto, T. A. D. S. Barros, M. V. de Paula, R. R. de Souza, and E. R. Filho, "Design of computational experiment for performance optimization of a switched reluctance generator in wind systems," *IEEE Trans. Energy Convers.*, vol. 33, no. 1, pp. 406–419, Mar. 2018.

[4] D. B. Wicklund and D. S. Zinger, "Voltage feedback signal conditioning in switched reluctance generation systems," in *Proc. 15th Annu. IEEE Appl. Power Electron. Conf. Expo. (APEC)*, vol. 1, Feb. 2000, pp. 376–380.

[5] K.-W. Hu, J.-C. Wang, T.-S. Lin, and C.-M. Liaw, "A switched-reluctance generator with interleaved interface DC–DC converter," *IEEE Trans. Energy Convers.*, vol. 30, no. 1, pp. 273–284, Mar. 2014.

[6] A. Klein-Hessling, B. Burkhart, and R. W. D. Doncker, "Active source current filtering to minimize the DC-link capacitor in switched reluctance drives," *CPSS Trans. Power Electron. Appl.*, vol. 4, no. 1, pp. 62–71, Mar. 2019.

[7] H. M. Hasanien and S. M. Muyeen, "Speed control of grid-connected switched reluctance generator driven by variable speed wind turbine using adaptive neural network controller," *Electr. Power Syst. Res.*, vol. 84, no. 1, pp. 206–213, Mar. 2012.

[8] S. M. Muyeen, A. Al-Durra, and H. M. Hasanien, "Application of an adaptive neuro-fuzzy controller for speed control of switched reluctance generator driven by variable speed wind turbine," in *Proc. Modern Electr. Power Syst. (MEPS)*, Jul. 2015, pp. 1–6.

[9] R. Cardenas, R. Pena, M. Perez, J. C. G. Asher, and P. Wheeler, "Control of a switched reluctance generator for variable-speed wind energy applications," *IEEE Trans. Energy Conver.*, vol. 20, no. 4, pp. 691–703, Dec. 2005.

[10] Y. C. Chang, C. H. Cheng, L. Y. Lu, and C. M. Liaw, "An experimental switched-reluctance generator based distributed power system," in *Proc. 19th Int. Conf. Electr. Mach. (ICEM)*, Sep. 2010, pp. 1–6.
[11] G. P. Viajante, D. A. Andrade, E. N. Chaves, V. R. Bernadelli, C. A. Queiroz, M. A. A. Freitas, J. A. Santos, and L. C. Gomes, "A grid connection scheme of a switched reluctance generator for active power injection using P-resonant (P-RES) controller," *Electr. Power Syst. Res.*, vol. 141, pp. 572–579, Dec. 2016.
[12] D. G. Photovoltaics and E. Storage, *IEEE Standard for Interconnection and Interoperability of Distributed Energy Resources With Associated Electric Power Systems Interfaces*, IEEE Standard 1547-2018, 2018.
[13] Y.-C. Chang and C.-M. Liaw, "On the design of power circuit and control scheme for switched reluctance generator," *IEEE Trans. Power Electron.*, vol. 23, no. 1, pp. 445–454, Jan. 2008.
[14] P. J. dos Santos Neto, T. A. D. S. Barros, E. H. Catata, and E. R. Filho, "Grid-connected SRG interfaced with bidirectional DC-DC converter in WECS," *IEEE Trans. Energy Convers.*, vol. 36, no. 4, pp. 3261–3270, Dec. 2021.
[15] A. Yazdani and R. Iravani, "An accurate model for the DC-side voltage control of the neutral point diode clamped converter," *IEEE Trans. Power Del.*, vol. 21, no. 1, pp. 185–193, Jan. 2005.
[16] A. Yazdani and R. Iravani, *Voltage-Sourced Converters in Power Systems: Modeling, Control, and Applications*. Hoboken, NJ, USA: Wiley, 2010.
[17] A. G. Yepes, "Digital resonant current controllers for voltage source converters," Ph.D. dissertation, Univ. Vigo, Vigo, Spain, 2011.
[18] C. Lascu, L. Asiminoaei, and F. Blaabjerg, "High performance current controller for selective harmonic compensation in active power filters," *IEEE Trans. Power Electron.*, vol. 22, no. 5, pp. 1826–1835, Sep. 2007.
[19] S. Golestan, M. Ramezani, J. M. Guerrero, F. D. Freijedo, and M. Monfared, "Moving average filter based phase-locked loops: Performance analysis and design guidelines," *IEEE Trans. Power Electron.*, vol. 29, no. 6, pp. 2750–2763, Jun. 2013.
[20] S. Golestan, M. Ramezani, J. M. Guerrero, and M. Monfared, "Dq-frame cascaded delayed signal cancellation-based PLL: Analysis, design, and comparison with moving average filter-based PLL," *IEEE Trans. Power Electron.*, vol. 30, no. 3, pp. 1618–1632, Mar. 2014.
[21] J. Svensson, M. Bongiorno, and A. Sannino, "Practical implementation of delayed signal cancellation method for phase-sequence separation," *IEEE Trans. Power Del.*, vol. 22, no. 1, pp. 18–26, Jan. 2006.

ELMER O. HANCCO CATATA (Member, IEEE) received the B.S. degree in electronic engineering from the National University of the Altiplano, Perú, in 2013, and the M.S. degree from the Federal University of ABC, Brazil, in 2016. He is currently pursuing the Ph.D. degree with the University of Campinas, Brazil. From 2017 to 2018, he was with the Electrical Engineering School, Federal University of Acre, Brazil. His research interests include renewable-energy systems, modeling and control of power electronic converters, and switched reluctance machines.

PEDRO JOSE DOS SANTOS NETO (Member, IEEE) received the B.S. degree in electrical engineering from the Federal University of Vale do Sao Francisco (UNIVASF), Petrolina, Brazil, in 2016, the M.S. degree from the University of Campinas (UNICAMP), Campinas, Brazil, in 2017, and the Ph.D. degree from UNICAMP, in 2021, under the São Paulo Research Foundation (FAPESP) Scholarship Program. In 2019, he was a Guest Ph.D. Visitor with the Center for Research on Microgrids (CROM), Aalborg University, Aalborg East, Denmark. He is currently a Professor with the Faculty of Electrical Engineering, Federal University of Uberlândia (UFU), Uberlândia, Brazil. He works in the areas of microgrids, electrical machines, and power electronics. His research interests include DC microgrids, renewable energy, and switched reluctance machines. He is a member of the Brazilian Society of Power Electronics (SOBRAEP).

MARCELO VINÍCIUS DE PAULA (Member, IEEE) received the B.S. degree in electrical engineering from the Federal University of Goiás, Brazil, in 2016, and the M.Sc. degree in electrical engineering from the University of Campinas, Campinas, Brazil, in 2018, where he is currently pursuing the Ph.D. degree, under the CNPq Scholarship Program. He involves in the areas of electric machines and drives, power electronics, and electric vehicles. His research interests include torque ripple minimization, switched reluctance machine drives, electric vehicles, and renewable energy.

JOÃO PEDRO CARVALHO SILVEIRA (Member, IEEE) received the B.S. degree in energy engineering and the M.S. degree in electrical engineering from the University of Brasilia (UnB), Brasilia, Brazil, in 2013 and 2016, respectively. He is currently pursuing the Ph.D. degree with the Power Electronics Laboratory (LEPO), University of Campinas, Campinas, Brazil, under the CAPES Scholarship Program. He works in the areas of electrical machines, power electronics, and electrical drives. His research interests include microgrids, energy storage systems, renewable energy, distributed generation, and power quality.

TÁRCIO ANDRÉ DOS SANTOS BARROS (Member, IEEE) received the B.S. degree in electrical engineering from the Federal University of Vale do São Francisco (UNIVASF), Petrolina, Brazil, in 2010, and the M.S. and Ph.D. degrees from the University of Campinas (UNICAMP), Campinas, Brazil, in 2012 and 2015, respectively. From 2016 to 2017, he was a Researcher with the Power Electronics Laboratory (LEPO), University of Campinas, under the FAPESP Postdoctoral Program. He is currently a Professor with the Mechanical Engineering Faculty, UNICAMP, and the Coordinating Member of the Brazilian Government Program ROTA 2030-FUNDEP (biofuel, vehicle safety, and alternative propulsion systems to combustion). He works in the areas of electrical machines, power electronics, electrical vehicles, and electrical drives. His research interests include machine drives, switched reluctance machines, doubly fed induction generators, and solar energy. He is a member of the Brazilian Society of Power Electronics (SOBRAEP).

ERNESTO RUPPERT FILHO (Member, IEEE) received the B.S. degree in electrical engineering and the M.S. and Ph.D. degrees from the University of Campinas (UNICAMP), Campinas, Brazil, in 1971, 1974, and 1983, respectively. From 1972 to 1978, he was with the Electrical and Computer Engineering School, UNICAMP, as an Assistant Professor of electromechanical energy conversion. From 1979 to 1983, he was with General Electric, Brazil, designing large induction and synchronous motors and working as an Application Engineer dedicated to large motors and generators. He is currently a Full Professor with the Electrical and Computer Engineering School, UNICAMP, researching and teaching in the areas of electrical machines, power electronics, drives, and electrical power systems.